THE JOURNAL OF PHYSICAL CHEMISTRY C
A JOURNAL OF THE AMERICAN CHEMICAL SOCIETY

pubs.acs.org/JPCC

Article

Stereochemically Active Lone Pairs: Unraveling the Electronic Origin of Dielectric Response in Nonlinear Optical TeO_2

Hoa H. Nguyen, Robin T. Macaluso, and Muhammad N. Huda*

Cite This: *J. Phys. Chem. C* 2024, 128, 1728−1736

Read Online

ACCESS | Metrics & More | Article Recommendations | Supporting Information

ABSTRACT: Tellurite glasses have emerged as a promising candidate for nonlinear optics (NLO) due to their high refractive index and third-order optical susceptibility (χ^3). In this work, we focus on the electronic structure of crystalline TeO_2, a precursor to numerous TeO_2-based glasses. All three crystalline TeO_2 polymorphs are wide-gap semiconductors and have electronic contributions from the Te^{4+} $5s^2$ lone pairs near the Fermi level, which affect optical properties. Based on the formation energies, the formation of oxygen vacancies is strongly favorable during synthesis. Introduction of an oxygen vacancy induces notable changes in the chemical environment in the pristine α-TeO_2 structure and the response of the Te $5s^2$ lone pairs. Comparative analysis to the measured refractive indices and static dielectric constant (a second-rank tensor) shows that the calculated values of α-TeO_2 with the presence of an oxygen vacancy (α-TeO_2:O_v) agree well with experimental data. The high distortion index and stereochemical activity ratio of α-TeO_2:O_v contribute to its polarizable asymmetric electron density. High polarization and faster orientation of the dipoles in α-TeO_2 with the presence of an oxygen vacancy make it an excellent NLO material for ultrafast optical switch applications. This study can help to guide design principles and improve our understanding of the electronic origin of NLO materials containing lone pairs.

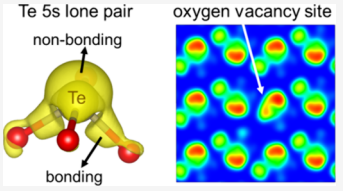

INTRODUCTION

Materials with nonlinear optical responses—where the polarization density responds nonlinearly to an electric field—have garnered significant interest in a variety of applications, ranging from wavelength conversion to telecommunications and optical computing.[1] Tellurite glasses have become promising candidates for nonlinear optics (NLO) due to their high refractive index (2.239 at 486.1 nm) and their third-order optical susceptibility (χ^3), on the order of 10^{-13} esu, considered to be the highest among oxides.[2,3] In particular, third-order optical nonlinearities and their dipole response times play a key role in high-frequency ultrafast optical switching.[1] For example, ZnO-Nb_2O_5-TeO_2 glasses have been investigated to display ultrafast nonlinear optical response (450 to 500 fs), which is desirable for optical switching applications.[4] One outstanding challenge in the field of NLO materials is the search for NLO-active materials in the infrared region, which would require less energy input compared to materials activated by UV−vis wavelengths.[5] With a large third-order optical susceptibility, TeO_2 can be considered a potential IR-active NLO material. Indeed, previous reports of NLO behavior at 800 and 1064 nm suggest the potential application of tellurite-based glass TeO_2−GeO_2−K_2O−Bi_2O_3 in the near-infrared region.[6]

Such promising NLO properties have motivated computational and experimental works in TeO_2-based materials. DFT +U studies comparing α-TeO_2 with β-TeO_3 indicate that the stereochemically active $5s^2$ lone pairs lead to a higher NLO susceptibility in α-TeO_2.[7,8] Thus, an effective NLO design strategy is to introduce stereochemically active lone pairs that results in structural distortions, asymmetric electron densities, and the formation of dipoles.[9] These polar behaviors are favorable for materials with NLO, particularly for compounds containing ions such as Pb^{2+}, As^{3+}, I^{5+}, Bi^{3+}, Te^{4+}, etc.[10−15]

Oxygen vacancies are one of the most common defects formed during the synthesis of metal oxides[16−18] and can have profound effects on material properties. The combination of lone pairs and vacancies is known to affect crystal structures and their optical and physical properties.[19,20] For example, defects such as zinc interstitials and oxygen vacancies enhanced third-order nonlinear parameters and optical response of $Zn_{(1-x)}Ni_xO$ nanoparticles and ZnO thin films.[21,22] Functional defects such as oxygen vacancies have been used to manipulate and tailor crystal structures, which provides more flexibility to control and enhance materials' properties. Specifically, oxygen vacancies in compounds with lone pairs can change the chemical environment around the atom, distorting the crystal structure and dipole orientations and varying the polarization responses. Therefore, a fundamental understanding of oxygen defects and their correlation to stereochemically active lone pairs will contribute significantly to understanding the synthesis of functional materials.

In this work, we focus on the electronic structure of crystalline TeO_2, which contains Te $5s^2$ lone pairs. We first

Received: August 13, 2023
Revised: December 13, 2023
Accepted: December 26, 2023
Published: January 18, 2024

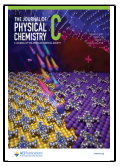

https://doi.org/10.1021/acs.jpcc.3c05472
J. Phys. Chem. C 2024, 128, 1728−1736

investigate the three known crystal structures and the stability of the crystalline TeO_2 phases, α-, β-, and γ-TeO_2, from first-principles calculations. We then primarily focus on the most common synthetic product—α-TeO_2. Characterization of the lone pairs in both pristine and oxygen-vacancy models is reported; in particular, we discuss their optoelectronic structures, distortion index (d), stereochemical activity ratio (R_{SCA}), and dielectric constant (ε). The goal of this paper is to understand the fundamentals of how the lone pair and oxygen vacancies impact NLO properties in crystalline TeO_2, so that we can ultimately target and design future TeO_2-based materials.

METHODS

Calculations. First-principles density functional theory (DFT)[23,24] calculations were performed using the Vienna Ab initio Simulation Package (VASP)[25−27] code and data postprocessing code VASPKIT.[28] The generalized-gradient approximation (GGA) with the exchange and correlation described by Perdew−Burke−Ernzerhof functionals was used.[29] For the core electrons of the atoms, the projected augmented wave[30,31] method was used. The electronic basis set was expanded with plane waves with a kinetic energy cutoff of 600 eV used throughout the calculations, affording well-converged results. Atomic position and volume were relaxed for each structure until the force on each ion was 0.01 eV/ Å or less. The zone-centered scheme was used to generate the k-point grid. A 15 × 15 × 10 k-point mesh was used for α-TeO_2, 12 × 12 × 6 k-point mesh for β-TeO_2, 10 × 10 × 5 for γ-TeO_2, and 3 × 3 × 3 for an oxygen vacancy containing 3 × 3 × 2 α-TeO_2 supercell. Due to the layered structure in β-TeO_2 and side chain interactions in α-TeO_2 and γ-TeO_2, geometry-dependent van der Waals correction[32,33] was applied for better optimization of all three TeO_2 polymorphs. Hybrid functionals[34] with 15% exact exchange and a 7 × 7 × 3 and 4 × 4 × 2 k-point mesh were employed to calculate the partial density of state (PDOS) for the α-TeO_2 and β-TeO_2, respectively, and to emphasize the localization of the lone pairs. Inclusion of spin−orbit coupling was also tested during the calculations; however, its effects on the electronic structure, specifically the Te $5s^2$ lone pairs, were not significant. The PDOS of α-TeO_2 using hybrid functionals with and without spin−orbit coupling are reported in the Supporting Information (Figure S1). Density functional perturbation theory[35,36] with GGA functionals was used to compute the static dielectric constants for the pristine α-TeO_2, β-TeO_2, and the oxygen vacancy containing α-TeO_2. The initial crystal structures of α-, β-, and γ-TeO_2 were obtained from the Materials Project.[37] The optical properties are determined by the real $\varepsilon_1(\omega)$ and imaginary $\varepsilon_2(\omega)$ parts of the dielectric constants. The absorption coefficients $\alpha(\omega)$ and refractive indices $n(\omega)$ are calculated by eqs 1 and 2, respectively:[38]

$$\alpha(\omega) = \frac{\sqrt{2}\,\omega}{c}[\sqrt{\varepsilon_1^{\,2}(\omega) + \varepsilon_2^{\,2}(\omega)} - \varepsilon_1(\omega)]^{1/2} \quad (1)$$

$$n(\omega) = \frac{[\sqrt{\varepsilon_1^{\,2}(\omega) + \varepsilon_2^{\,2}(\omega)} + \varepsilon_1(\omega)]^{1/2}}{\sqrt{2}} \quad (2)$$

Diffuse Reflectance Spectroscopy (DRS). Indirect and direct optical band gaps of α-TeO_2 (99.99%, Alfa Aesar) were estimated by DRS measurements and Tauc analyses.[39,40] DRS data were collected with wavelengths ranging from 200 to 700 nm using a PerkinElmer Lambda 365 UV/vis spectrophotometer equipped with an integrating sphere. The reflectance measurements were converted to the Kubelka−Munk function defined as $F(R) = \alpha/S = (1 - R)^2/2R$, where α is the absorption coefficient, S is the scattering coefficient, and R is the reflectance at a given wavelength.[39,41] The Tauc plot is constructed based on the equation $(F(R)h\nu)^n = B(h\nu - E_g)$, where B is a proportionality constant, E_g represents the energy (optical) band gap, and n denotes the mode of electronic transition, $n = 1/2$ for indirect transition and $n = 2$ for direct transition in α-TeO_2.[41]

RESULTS AND DISCUSSION

Crystal Structure and Thermal Stability of TeO_2 Polymorphs. The three known tellurium dioxide polymorphs are α-TeO_2, β-TeO_2, and γ-TeO_2. The structures of all three polymorphs were relaxed to minimize the interatomic forces and optimize the lattice parameters. Table 1 summarizes the crystal structures and calculated and experimental structural data for all three TeO_2 polymorphs. Paratellurite, α-TeO_2, adopts the noncentrosymmetric $P4_12_12$ space group; tellurite, β-TeO_2, adopts the orthorhombic $Pbca$ space group; and γ-TeO_2 adopts the orthorhombic $P2_12_12_1$ space group. The α-TeO_2 structure is constructed of helical chains of corner-sharing TeO_4 disphenoids along the c-direction. In both experimental and calculated models, each TeO_4 disphenoid in α-TeO_2 has two longer axial and two shorter equatorial Te−O bonds. The β-TeO_2 structure is composed of edge-sharing TeO_4 disphenoid layers where each disphenoid has four different Te−O bond lengths consisted of two short equatorial and two longer axial Te−O bonds. Finally, γ-TeO_2 contains chains of TeO_3 polyhedra. In contrast to the disphenoids in α- and β-TeO_2, one of the Te−O bonds in the TeO_4 disphenoid of γ-TeO_2 has a much longer bond length of 2.256 Å and is considered nonbonding. Therefore, each Te atom in γ-TeO_2 is coordinated to only three oxygen atoms.

Table 1. Calculated and Experimental Structural Data for TeO_2 Polymorphs

	Crystal Structure	Structural Data	Experimental[42-44] (Å)	Computational (Å)	Difference (%)
α-TeO_2		a, b	4.808	4.800	0.173
		c	7.612	7.345	3.512
		Te−O distances	2.121	2.144	1.063
			1.879	1.928	2.590
β-TeO_2	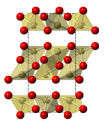	a	5.464	5.446	0.330
		b	5.607	5.703	1.717
		c	12.035	11.776	2.155
		Te−O distances	2.070	2.087	0.815
			2.196	2.157	1.748
			1.927	1.940	0.668
			1.877	1.926	2.603
γ-TeO_2	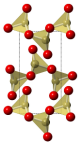	a	4.898	4.897	0.018
		b	4.351	4.276	1.727
		c	8.576	8.596	0.236
		Te−O distances	2.019	2.049	1.486
			2.197	2.256	2.671
			1.860	1.872	0.697
			1.948	1.958	0.505

Because of the layer and chain features in α-, β-, and γ-TeO_2, van der Waals interactions were included for better structural relaxation of all three polymorphs. Inclusion of van der Waals corrections in α-TeO_2 resulted in a and b lattice parameters that are similar to experimental lattice parameters; however, the calculated c lattice parameter is underestimated when compared to experimental lattice parameters (Table 1). Since

https://doi.org/10.1021/acs.jpcc.3c05472
J. Phys. Chem. C 2024, 128, 1728−1736

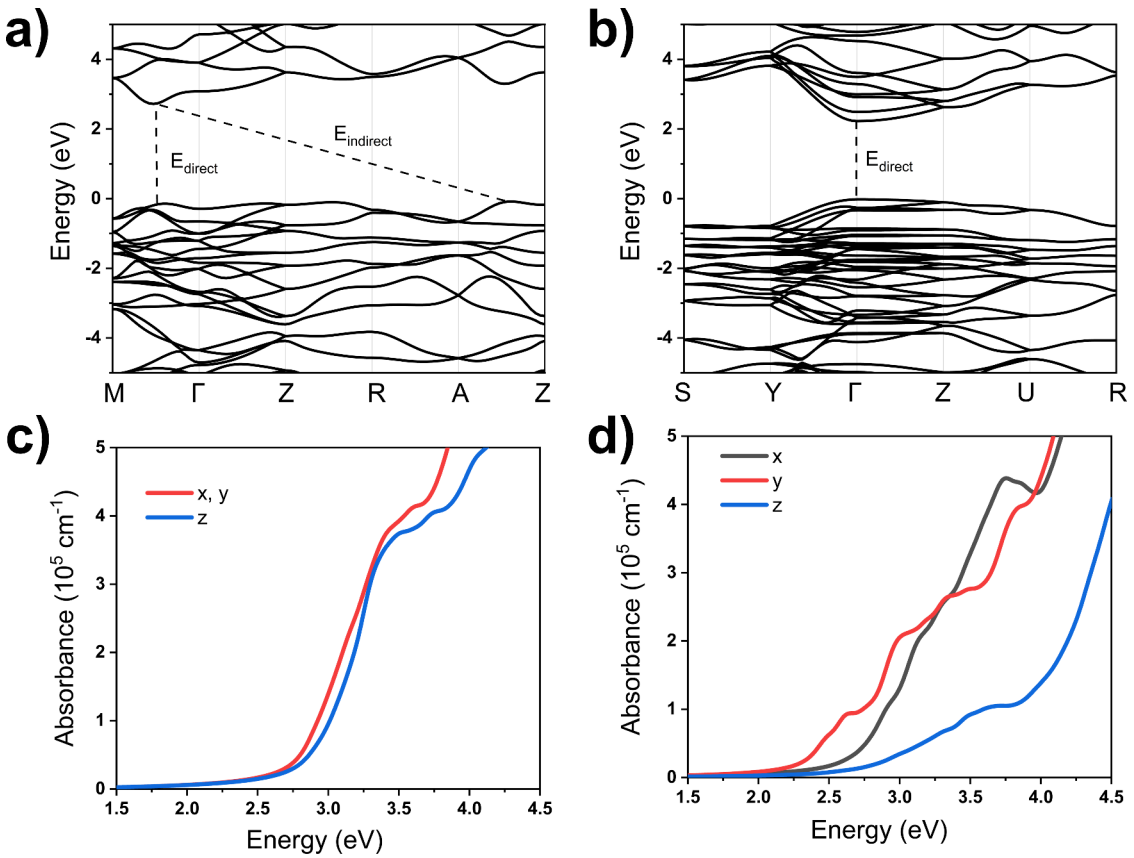

Figure 1. Electronic band structures of TeO_2 polymorphs (a) α-TeO_2 and (b) β-TeO_2 and optical absorption plots of (c) α-TeO_2 and (d) β-TeO_2 generated with GGA functionals. For the band structures, 0 eV is the highest occupied band.

the chains are along the *c*-direction, the side chain interactions in the *ab*-plane are corrected appropriately, while the *c* lattice parameter is compressed. The van der Waals corrections were added to β-TeO_2 calculations to accommodate the weak interactions between TeO_4 disphenoid layers and to improve model fidelity. The average difference between the calculated lattice constants and bond lengths from experimental data is 1.373% with a maximum of 3.512%. The overall small differences between experimental versus our calculated values demonstrate reliability of our calculations.

After obtaining the relaxed structure for all three polymorphs, the formation enthalpy of each polymorph was then calculated by eq 3:

$$E_f(TeO_2) = E_t(TeO_2) - E_t(\text{Te bulk}) - E_t(O_2) \quad (3)$$

where $E_t(TeO_2)$ is the total energy of pristine TeO_2 of the polymorph, E_t(Te bulk) is the total energy of tellurium in its bulk phase, and $E_t(O_2)$ is the total energy of an oxygen molecule in the triplet state. According to the calculated formation energies, β-TeO_2 is the most stable with the lowest formation energy of −3.616 eV/f.u., followed by α-TeO_2 with a formation energy of −3.582 eV/f.u., and finally γ-TeO_2 with the highest formation energy of −3.571 eV/f.u. β-TeO_2 exists as the tellurite mineral in nature,[43] and the addition of weak van der Waals interactions between TeO_4 layers contributed to its low formation energy and high thermodynamic stability. Paratellurite (α-TeO_2) is synthetically the most stable and used in many optical technologies and as a precursor for many glass-based applications. A previous dispersion corrected GGA study also determined α-TeO_2 to be the most thermochemically stable based on formation energies.[45] Because the absence of an inversion center in the structure favors NLO behavior, the Results and Discussion section of this paper primarily focuses on α-TeO_2. The β-TeO_2 structure is the most thermodynamically stable polymorph and belongs to a centrosymmetric space group. Therefore, comparison of the electronic structure of centrosymmetric β-TeO_2 and noncentrosymmetric α-TeO_2 is beneficial to studying polarization, which is the source of NLO. Note that, though noncentrosymmetric in nature, α-TeO_2 is not known for second harmonic generation. In the next parts, we will be discussing the electronic structures of the noncentrosymmetric pristine α-TeO_2, centrosymmetric β-TeO_2, and oxygen vacancy α-TeO_2 with the focus on the effects of the stereochemical activity of Te lone pairs and their correlation with oxygen vacancy on the structure and optoelectronic properties.

Pristine α-TeO_2 and β-TeO_2. The electronic band structures of α-TeO_2 and β-TeO_2 were calculated with GGA functionals (Figure 1) where the Fermi level (0 eV) was defined as the highest occupied state. The band gap of α-TeO_2 (Figure 1a) was determined to be indirect with a value of 2.761 eV from the valence band maximum (VBM) between the A and Z symmetry points to the conduction band minimum (CBM) between the M and Γ symmetry points. A direct band gap of α-TeO_2 was determined to be 2.919 eV at the top of the valence band to the CBM. Figure 1b shows that the β-TeO_2 has a direct band gap at the Γ symmetry point of 2.141 eV. The band structures of both α- and β-TeO_2 agree with previously reported band structures.[46−48] The computed optical band gaps of α-TeO_2 and β-TeO_2 (Figure 1c,d)

https://doi.org/10.1021/acs.jpcc.3c05472
J. Phys. Chem. C 2024, 128, 1728−1736

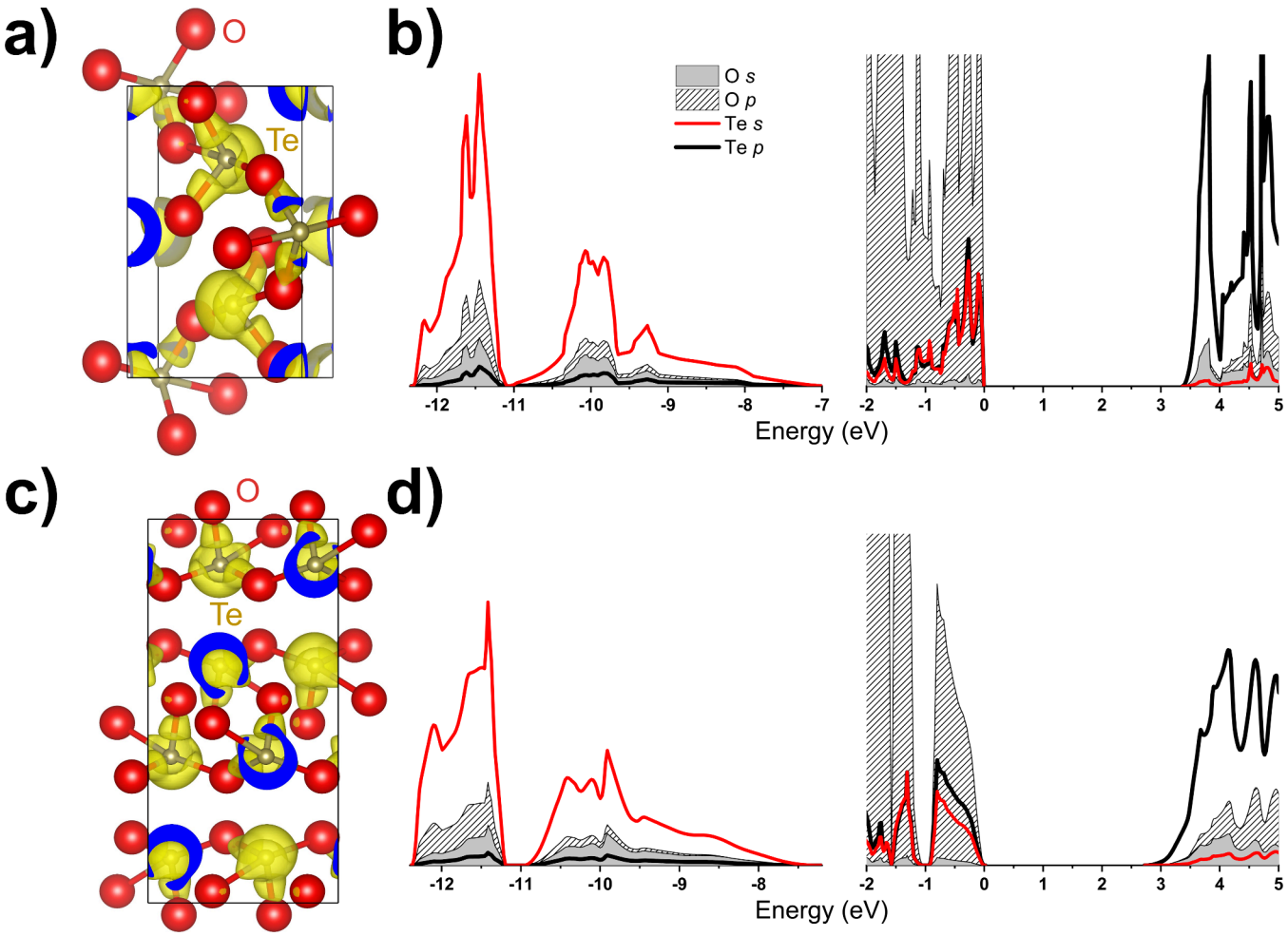

Figure 2. Charge density plot of Te and Te−O bondings in (a) α-TeO_2 and (c) β-TeO_2 coupled with PDOS plots for (b) α-TeO_2 and (d) β-TeO_2 using hybrid functionals. Note that the discontinuity on the energy axis (horizontal axis) is included to enhance the features of the PDOS plots.

indicate direct band gaps of ~3.0 and 2.2 eV, respectively, and agree well with the direct band gap extrapolated from the band structures. The calculated α-TeO_2 band gap underestimates our experimental values of 3.45 and 3.79 eV for indirect and direct gaps, respectively (Figure S2). This band gap underestimation is a well-known limitation of DFT using GGA functionals. The β-TeO_2 direct band gap was slightly lower than a previously calculated band gap of ~2.2 eV.[46,48]

Since, to the best of our knowledge, there are no other experimental characterizations for the electronic structure of α-TeO_2 and β-TeO_2 other than the optical band gap, we adopted hybrid functionals with spin polarization to determine whether the calculated band gaps come closer to the experimental band gap. The calculated PDOS plots and band structure for α-TeO_2 using hybrid functionals (Figure 2b and Figure S3) show an increase in the band gap from 2.761 to 3.418 eV for α-TeO_2. The experimental and computational band gap values of α-TeO_2 are summarized in Table 2. Larger band gap values with the use of hybrid functionals reflect a more accurate experimental band gap (3.45 eV) of α-TeO_2. The band gap also increases from 2.141 to 2.748 eV for β-TeO_2 (Figure 2d). The addition of exact exchange in hybrid functionals also benefits our study of lone pairs by increasing the localization to the orbitals.

The PDOS of α-TeO_2 and β-TeO_2 are similar where Te $5s^2$ lone pairs contribute mostly from the energy region of −12 to −7.5 eV together with O $2p$ and O $2s$ and very small contributions of Te $5p$ states. The contribution of the Te^{4+} lone pairs is shown within the two peaks. A more intense and sharper peak at approximately −11 to −12 eV represents a localized and inert part of the orbital, which is displayed as the spherical portion toward the nonbonding direction of tellurium atoms in the charge density plot for both α-TeO_2 and β-TeO_2 (Figure 2a,c). Meanwhile, another broader Te $5s^2$ peak at around −11 to −7 eV indicates the delocalized part of the s orbital where it contributes toward the Te−O bonding. The assignment of the localized and delocalized part of the Te 5s orbital becomes evident when manipulating the layer separation in β-TeO_2 (Figure S4). A compression and expansion of the interlayer separation of β-TeO_2 was constructed, and the PDOS are shown in the Supporting Information (Figure S4). In the pristine β-TeO_2 structure, the layer separation is 1.916 Å. The distance between the layers in

Table 2. Summary of Experimental and Calculated Band Gaps of α-TeO_2

	experimental	calculated using GGA functionals	calculated using hybrid functionals
direct band gap (eV)	3.79	2.761	3.418
indirect band gap (eV)	3.45	2.919	3.585

https://doi.org/10.1021/acs.jpcc.3c05472
J. Phys. Chem. C 2024, 128, 1728−1736

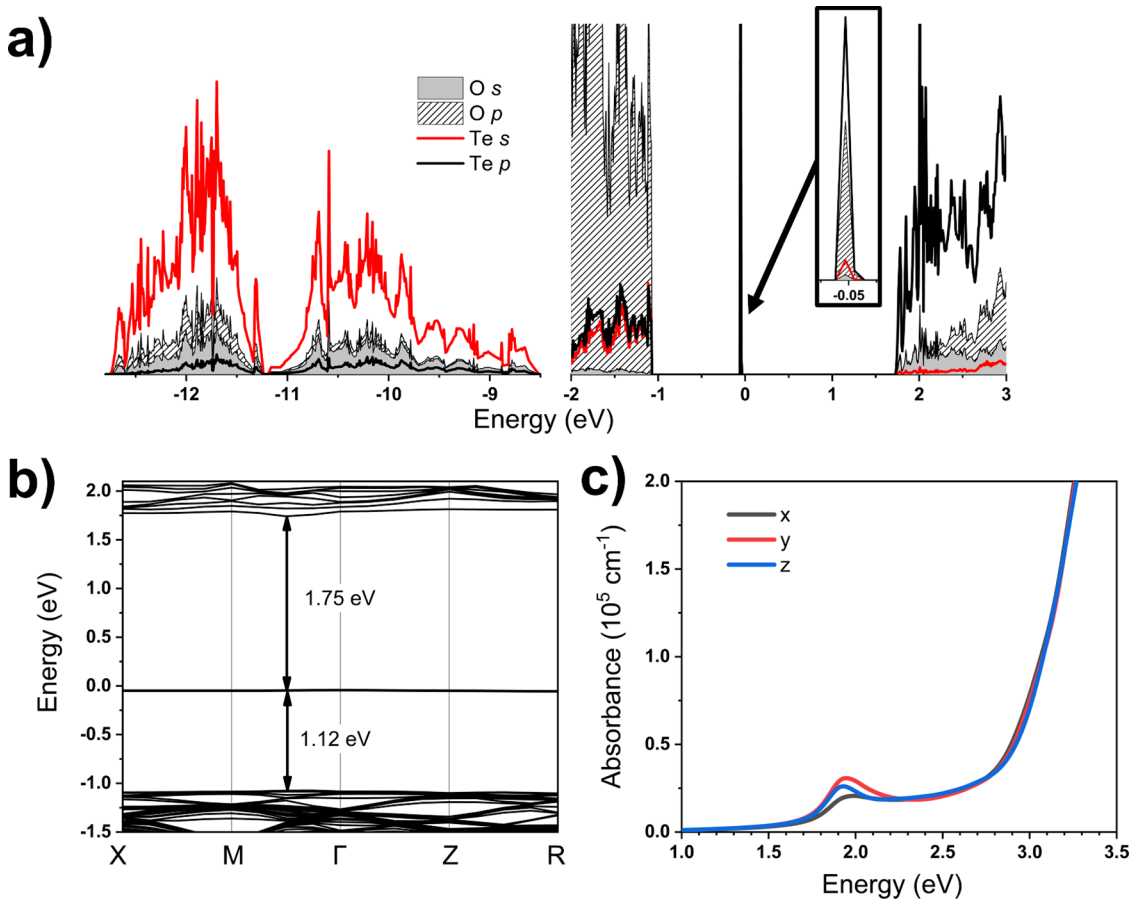

Figure 3. (a) PDOS plot, (b) band structure, and (c) optical absorption plot of O-vacancy containing TeO2, α-TeO2:O_v, using GGA functionals. Both the band structure and DOS plot show the occupied defect level due to the oxygen vacancy. The Fermi level, the highest occupied band, is scaled to 0 eV on the PDOS plots and band structure. Note that the discontinuity on the energy axis (horizontal axis) is included to enhance the features of the PDOS plots.

β-TeO_2 was decreased and increased by 0.7 Å in the compressed and expanded β-TeO_2 model, respectively. Increasing the interlayer distance reduces the interaction of the lone pairs between the layers, making them more localized and inert. Therefore, the localized nature of the lone pair is represented by the sharper, more intense peak at approximately −12 to −11 eV.

The O 2*p* states dominate around the Fermi energy; however, the Te $5s^2$ lone pairs also contribute to the VBM. The interlayer interaction between Te 5*s* lone pairs in β-TeO_2 (Figure 2c) results in an additional feature between −1 and 0 eV in the PDOS of β-TeO_2 (Figure 2d). This feature is not observed in α-TeO_2 (Figure 2b). Therefore, adjusting the separation between two layers will have consequences for the interaction between lone pairs. By decreasing the interlayer distance, the repulsion between Te 5*s* lone pairs will result in highly localized lone pairs. A sharp high-intensity peak should be observed at the top of the valence band, as seen in Figure S4. The lone pair contribution is shown at the top valence band in both α- and β-TeO_2, which indicates stereochemically active lone pairs in both polymorphs. However, due to the interlayer interaction of the Te lone pairs in β-TeO_2, the contribution of the lone pair to bonding with oxygen in β-TeO_2 is less than that in α-TeO_2, resulting in lower stereochemical activity of Te lone pairs in β-TeO_2. Nevertheless, in the charge density plot of α-TeO_2 and β-TeO_2 (Figure 2a,c), the Te $5s^2$ orbital is not found as a complete and isolated sphere but rather a semispherical shape around the tellurium atom, making Te $5s^2$ stereochemically active and not simply taking up empty space.

Oxygen Vacancy in α-TeO_2. Common synthetic methods for α-TeO_2 yield products with a Te:O molar fraction greater than the ideal 1:2 molar ratio, indicating the presence of oxygen vacancies.[49] Hence, we consider oxygen vacancies in TeO_2 denoted as α-TeO_2:O_v. Such vacancies are known to affect the electronic and optical properties. In addition, oxygen vacancies are expected to alter the local Te environment. The formation energy of an oxygen vacancy in α-TeO_2 was calculated using eq 4:

$$E_f(TeO_2{:}\ O_v) = E_t(TeO_2{:}\ O_v) - E_t(TeO_2) + \frac{1}{2}E_t(O_2) + \Delta\mu_O \quad (4)$$

where $E_f(TeO_2{:}O_v)$ is the total energy of α-TeO_2 with an O vacancy, $E_t(TeO_2)$ is the total energy of the pristine α-TeO_2, $E_t(O_2)$ is the total energy of the oxygen dimer in the triplet state, and $\Delta\mu_O$ is the change in oxygen chemical potential that reflects the oxygen environment in the synthesis condition such as an oxygen-rich or poor condition. The $\Delta\mu_O$ is bounded by the following:

$$\frac{1}{2}E_f(TeO_2) \le \Delta\mu_O \le 0 \quad (5)$$

https://doi.org/10.1021/acs.jpcc.3c05472
J. Phys. Chem. C 2024, 128, 1728−1736

where an oxygen-poor synthesis condition is defined as $\Delta\mu_O = \frac{1}{2}E_f(TeO_2)$ and an oxygen-rich condition is defined as $\Delta\mu_O = 0$. The calculated formation energies of α-TeO_2:O_v are −6.688 and −4.897 eV/f.u. under oxygen-poor and oxygen-rich conditions, respectively. The largely negative values of $E_f(TeO_2)$ indicate that oxygen vacancy formation is thermodynamically favorable.

Previously, the refractive indices of paratellurite α-TeO_2 crystal were measured at 1.94 eV with the values of 2.2565 for the ordinary refractive index (n_o) and 2.4088 for the extraordinary refractive index (n_e).[50] In comparing the measured refractive indices at 1.94 eV with the computed data extracted from the refractive index plots (Figure S5) (n_o = 2.7320 and n_e = 2.8966) for the pristine α-TeO_2 and (n_o = 2.4808 and n_e = 2.6618) for α-TeO_2:O_v, the calculated refractive indices of α-TeO_2:O_v are closer to the experimental data, which emphasizes the favorable formation of oxygen vacancies in the synthesized single crystal.

The PDOS of α-TeO_2:O_v (Figure 3a) shows that the contribution of Te $5s^2$ lone pairs at around −12 to −7 eV is still present; however, their peak intensities and shapes vary compared to those of pristine α-TeO_2. The participation of tellurium lone pairs in bonding is affected by the new chemical environment when inducing an oxygen vacancy in the structure. This is also shown in the electron localization functions. In the pristine α-TeO_2, the lone pair density is shown on the Te atoms with *s* orbital-like nature (Figure 4a,c).

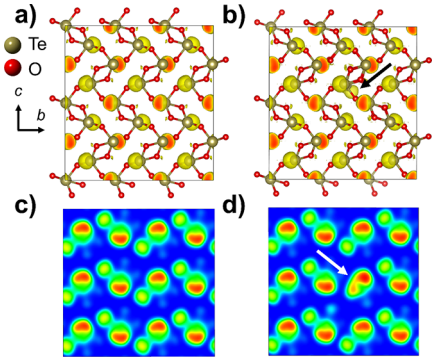

Figure 4. Electron localization functions along with the 2D slice at the (200) plane containing the vacancy site (indicated with an arrow) of (a, c) pristine α-TeO_2 and (b, d) α-TeO_2:O_v.

Upon introduction of an oxygen vacancy (Figure 4b,d), the lone pair electron density around the Te atom is delocalized, creating an asymmetric charge density at the vacancy site. This asymmetric charge density can contribute to the polarization and the observation of the NLO behavior in α-TeO_2.

Besides charge density, the oxygen vacancy also alters the optical properties of α-TeO_2. Due to the oxygen vacancy, there is an occupied defect state between the VBM and CBM, as shown in the PDOS and the band structure (Figure 3a,b), causing an additional absorption peak at a lower energy in the absorption plot (Figure 3c) where an electron is excited with 1.8 eV to transition from the defect state to the CBM and another excitation of 2.9 eV from the top of the valence band to the CBM.

Stereochemical Activity of Te $5s^2$ Lone Pairs. To quantitatively investigate the distortion caused by the stereochemically active lone pairs, we studied the bond distortion index in the TeO_4 disphenoids. The bond length distortion index, *d*,[51] is defined in eq 6:

$$d = \frac{1}{n}\sum_i^n \frac{|l_i - l_{avg}|}{l_{avg}} \quad (6)$$

where l_i is the bond length from the central Te atom to the *i*th coordinating oxygen and l_{avg} is the average bond length of Te−O bonds within the polyhedron. The distortion indices *d* of α-TeO_2, β-TeO_2, and α-TeO_2:O_v are shown in Table 3.

Table 3. Distortion Indices (d) and Stereochemical Activity (R_{SCA}) of Te $5s^2$ Lone Pairs in α-TeO_2, β-TeO_2, and α-TeO_2:O_v

	d	R_{SCA}
α-TeO_2	0.053	0.990
β-TeO_2	0.047	0.764
α-TeO_2:O_v	0.056	1.018

Introducing an oxygen vacancy in α-TeO_2 distorts all of the polyhedra in the supercell, and variation of the distortion index for each polyhedron depends on its proximity to the vacancy site. Therefore, taking an average of the distortion index for all polyhedra in the α-TeO_2:O_v supercell will give an estimate of the overall distortion index in the supercell.

The revised lone pair model[52] suggested that the stereochemically active 5*s* lone pairs of the cation strongly interact with anion *p* orbitals, creating bonding and antibonding states. Their antibonding states are seen at the VBM in the PDOS plot.[52] This implies that a larger contribution of the cation *s* orbital to the top of the valence band results in an increased stereochemical activity of the lone pairs. In addition, structural distortion will allow the unoccupied cation *p* states to interact with the antibonding of cation *s* and anion *p* orbitals, resulting in a further stabilization of the occupied electronic states, which induces the stereochemical activity of the lone pairs (Figure S6). Therefore, a comparison between the contributions of Te-*s* and Te-*p* near the Fermi level can characterize the degree of the stereochemical activity (SCA) of Te $5s^2$, which has previously been defined as an R_{SCA} ratio[14,15] shown in eq 7:

$$R_{SCA} = \frac{I_{Te5s}}{I_{Te5p}} \quad (7)$$

where $I_{Te\ 5s}$ and $I_{Te\ 5p}$ are the area under the curve in the PDOS plot of Te-*s* and Te-*p* orbitals within an energy range from the Fermi level to where their intensities are equal. This represents the number of electrons that the Te-*s* and Te-*p* orbitals contributed at the top of the valence band. The larger the R_{SCA} ratio, the greater the contribution of the lone pairs to the antibonding state with the anion *p* orbital, which increases the SCA of the lone pairs. The R_{SCA} for α-TeO_2, β-TeO_2, and α-TeO_2:O_v are recorded in Table 3. A higher distortion index and stereochemical activity R_{SCA} of Te $5s^2$ indicates that the stereochemical active lone pairs in α-TeO_2 with an oxygen vacancy create more distortion on its TeO_4 disphenoids. Thus, this distortion can give rise to a more asymmetric electron density, resulting in high third-order optical susceptibility compared to the pristine α-TeO_2 and the centrosymmetric β-TeO_2.

The dielectric constant is related to the degree of polarization of a material, which is a crucial property in NLO. The calculated diagonal dielectric tensors of α-TeO_2, α-

https://doi.org/10.1021/acs.jpcc.3c05472
J. Phys. Chem. C 2024, 128, 1728−1736

TeO_2:O_v, and β-TeO_2 are recorded in Table 4. The static dielectric constants are the sum of the electronic and ionic/lattice dielectric constants at a static field (E = 0 eV), which is extrapolated from Figure S7. The dielectric constants of the single crystal α-TeO_2 were measured in a previous study to be 22.9 and 24.7 in the x and y directions, respectively.[53] The dielectric constant of 20 was also measured for the crystalline α-TeO_2 over the frequency range from 400 Hz to 1 MHz.[54] The experimentally determined dielectric constants of crystal and powder α-TeO_2 are on the same order of magnitude with the computed dielectric constant of α-TeO_2 with an oxygen vacancy. This reinforces the possibility of oxygen vacancies in synthesized α-TeO_2. When an electric field (E) is applied, the electric polarization vector $\boldsymbol{P}$ is defined as $\boldsymbol{P} = \varepsilon_0\chi_e E$, where $\chi_e E$ can be expanded in higher-order terms.[55] The polarization $\boldsymbol{P}$ is correlated to the dielectric constant. Tellurium dioxide has a relatively high dielectric constant, around 5 times the dielectric constant of silicon dioxide, a conventional glass material.[56] This gives rise to a higher polarization and NLO in the TeO_2 glass. Another aspect to consider besides a high polarization in NLO materials is how fast the dipoles reorient under an applied rapidly changing electric field. Since the dielectric constant is directly correlated to resistive-capacitive time delay, a lower ε, and thus lower capacitance, should correspond to a faster reorientation of the dipoles under an applied electric field. Relatively lower static dielectric constants of α-TeO_2:O_v compared to pristine α- TeO_2 indicate that the presence of oxygen vacancy in α-TeO_2 can reduce the reorientation time of the dipoles and increase the NLO response time. This can help to guide the synthesis and tune the NLO response of future TeO_2-based materials.

Table 4. Summary of the Calculated Dielectric Tensors of α-TeO_2, α-TeO_2:O_v, and β-TeO_2

	α-TeO_2	α-TeO_2:O_v	β-TeO_2
ε_{xx}	32.835	26.816	26.267
ε_{yy}	32.835	26.832	24.416
ε_{zz}	35.801	36.665	10.577

CONCLUSIONS

First-principles calculations were used to investigate the structural, electronic, and optical properties of α-TeO_2, β-TeO_2, γ-TeO_2, and α-TeO_2:O_v. Thermodynamic stabilities of three TeO_2 polymorphs are ranked β-TeO_2 > α-TeO_2 > γ-TeO_2 based on their calculated formation energies. Hybrid functionals were employed to enhance the band gap accuracy compared to the experimental values and the localization of the Te $5s^2$ lone pairs. The band gaps for α-TeO_2 and β-TeO_2 were determined to be 3.418 eV (indirect) and 2.748 eV (direct), respectively, using hybrid functionals. The presence of an oxygen vacancy has been shown to be very favorable in α-TeO_2 with the formation energies of −4.897 eV/f.u. under an oxygen-rich synthesis condition and −6.688 eV/f.u. under an oxygen-poor synthesis condition. Due to the overlap of Te 5s with O 2p at the VBM, the partially delocalized Te 5s orbital contributes to Te−O bonds. Their response to changes in the chemical environment, such as oxygen vacancy formation, indicates that Te $5s^2$ electrons are stereochemically active lone pairs. The stereochemical activity (SCA) of lone pairs was quantified by determining the ratio of tellurium s and p orbitals at the top of the valence band. In the presence of an oxygen vacancy, α-TeO_2:O_v has a high distortion index and stereochemical activity ratio, which distorts TeO_4 disphenoids, creating a highly polarizable asymmetric electron density. A relatively lower dielectric constant of α-TeO_2:O_v compared to the pristine α-TeO_2 suggests a faster reorientation of the dipoles under an applied electric field, which suggests that α-TeO_2:O_v could be an excellent candidate for ultrafast optical switch applications. This study of stereochemically active lone pairs and oxygen vacancy in TeO_2 provides useful insight into an electronic origin of NLO properties in the crystalline phase, which can guide design principles for future TeO_2-based NLO materials.

ASSOCIATED CONTENT

Supporting Information

The Supporting Information is available free of charge at https://pubs.acs.org/doi/10.1021/acs.jpcc.3c05472.

Partial density of state plots of α-TeO_2 with and without spin−orbit coupling; Tauc analysis to determine the direct and indirect band gap of α-TeO_2; band structure of α-TeO_2 using hybrid functionals; partial density of state plots for compressed, pristine, and expanded layer β-TeO_2; refractive indices with respect to energy plots of α-TeO_2 and α-TeO_2:O_v; molecular orbital diagram of Te and O; real part of electronic and ionic/lattice contributions with respect to energy plots of α-TeO_2 and α-TeO_2:O_v (PDF)

AUTHOR INFORMATION

Corresponding Author

Muhammad N. Huda − *Department of Physics, University of Texas at Arlington, Arlington, Texas 76019, United States;* orcid.org/0000-0002-2655-498X; Email: huda@uta.edu

Authors

Hoa H. Nguyen − *Department of Chemistry and Biochemistry, University of Texas at Arlington, Arlington, Texas 76019, United States;* orcid.org/0000-0002-3375-4998

Robin T. Macaluso − *Department of Chemistry and Biochemistry, University of Texas at Arlington, Arlington, Texas 76019, United States;* orcid.org/0000-0002-0021-0775

Complete contact information is available at: https://pubs.acs.org/10.1021/acs.jpcc.3c05472

Notes

The authors declare no competing financial interest.

ACKNOWLEDGMENTS

This work was supported by the National Science Foundation Division of Materials Research (NSF DMR 2113689) and the UTA/NU Partnership for Research and Education in Materials (NSF DMR-2122128). The computations were performed at the Texas Advanced Computing Center (TACC).

REFERENCES

(1) Suresh, S.; Ramanand, A.; Jayaraman, D.; Mani, P. Review on Theoretical Aspect of Nonlinear Optics. *Rev. Adv. Mater. Sci.* **2012**, *30*, 175−183.

(2) Kim, S.-H.; Yoko, T.; Sakka, S. Linear and Nonlinear Optical Properties of TeO_2 Glass. *J. Am. Ceram. Soc.* **1993**, *76* (10), 2486−2490.

(3) Dussauze, M.; Cremoux, T.; Adamietz, F.; Rodriguez, V.; Fargin, E.; Yang, G.; Cardinal, T. Thermal Poling of Optical Glasses: Mechanisms and Second-Order Optical Properties. *Int. J. Appl. Glass Sci.* **2012**, *3* (4), 309−320.
(4) Lin, J.; Huang, W.; Sun, Z.; Ray, C. S.; Day, D. E. Structure and Non-linear Optical Performance of TeO_2-Nb_2O_5-ZnO Glasses. *J. Non-Cryst. Solids* **2004**, *336* (3), 189−194.
(5) Abudurusuli, A.; Li, J.; Pan, S. A Review on the Recently Developed Promising Infrared Nonlinear Optical Materials. *Dalton Trans.* **2021**, *50* (9), 3155−3160.
(6) Oliveira, T. A.; Manzani, D.; Falcão-Filho, E. L.; Messaddeq, Y.; Boudebs, G.; Fedus, K.; de Araújo, C. B. Near-infrared Nonlinearity of a Multicomponent Tellurium Oxide Glass at 800 and 1,064 nm. *Appl. Phys. B: Laser Opt.* **2014**, *116* (1), 1−5.
(7) Roginskii, E. M.; Kuznetsov, V. G.; Smirnov, M. B.; Noguera, O.; Duclère, J. R.; Colas, M.; Masson, O.; Thomas, P. Comparative Analysis of the Electronic Structure and Nonlinear Optical Susceptibility of α-TeO_2 and β-TeO_3 Crystals. *J. Phys. Chem. C* **2017**, *121* (22), 12365−12374.
(8) Suehara, S.; Thomas, P.; Mirgorodsky, A.; Merle-Méjean, T.; Champarnaud-Mesjard, J. C.; Aizawa, T.; Hishita, S.; Todoroki, S.; Konishi, T.; Inoue, S. Non-linear Optical Properties of TeO_2-based Glasses: ab initio Static Finite-field and Time-dependent Calculations. *J. Non-Cryst. Solids* **2004**, *345*−*346*, 730−733.
(9) Laurita, G.; Seshadri, R. Chemistry, Structure, and Function of Lone Pairs in Extended Solids. *Acc. Chem. Res.* **2022**, *55* (7), 1004−1014.
(10) Huang, Y.-Z.; Wu, L.-M.; Wu, X.-T.; Li, L.-H.; Chen, L.; Zhang, Y.-F. $Pb_2B_5O_9I$: An Iodide Borate with Strong Second Harmonic Generation. *J. Am. Chem. Soc.* **2010**, *132* (37), 12788−12789.
(11) Nguyen, S. D.; Yeon, J.; Kim, S.-H.; Halasyamani, P. S. $BiO(IO_3)$: A New Polar Iodate that Exhibits an Aurivillius-Type $(Bi_2O_2)^{2+}$ Layer and a Large SHG Response. *J. Am. Chem. Soc.* **2011**, *133* (32), 12422−12425.
(12) Zou, G.; Huang, L.; Ye, N.; Lin, C.; Cheng, W.; Huang, H. $CsPbCO_3F$: A Strong Second-Harmonic Generation Material Derived from Enhancement via p−π Interaction. *J. Am. Chem. Soc.* **2013**, *135* (49), 18560−18566.
(13) Hellwig, H.; Liebertz, J.; Bohatý, L. Exceptional Large Nonlinear Optical Coefficients in the Monoclinic Bismuth Borate BiB_3O_6 (BIBO). *Solid State Commun.* **1998**, *109* (4), 249−251.
(14) Yin, R.; Hu, C.; Lei, B.-H.; Pan, S.; Yang, Z. Lone Pair Effects on Ternary Infrared Nonlinear Optical Materials. *Phys. Chem. Chem. Phys.* **2019**, *21* (9), 5142−5147.
(15) Hu, C.; Mutailipu, M.; Wang, Y.; Guo, F.; Yang, Z.; Pan, S. The Activity of Lone Pair Contributing to SHG Response in Bismuth Borates: a Combination Investigation from Experiment and DFT Calculation. *Phys. Chem. Chem. Phys.* **2017**, *19* (37), 25270−25276.
(16) Merkle, R.; Maier, J. How Is Oxygen Incorporated into Oxides? A Comprehensive Kinetic Study of a Simple Solid-State Reaction with $SrTiO_3$ as a Model Material. *Angew. Chem., Int. Ed.* **2008**, *47* (21), 3874−3894.
(17) Ganduglia-Pirovano, M. V.; Hofmann, A.; Sauer, J. Oxygen Vacancies in Transition Metal and Rare Earth Oxides: Current State of Understanding and Remaining Challenges. *Surf. Sci. Rep.* **2007**, *62* (6), 219−270.
(18) Kennedy, B. J. Oxygen Vacancies in Pyrochlore Oxides: Powder Neutron Diffraction Study of $Pb_2Ir_2O_{6.5}$ and $Bi_2Ir_2O_{7-y}$. *J. Solid State Chem.* **1996**, *123* (1), 14−20.
(19) Reshak, A. H.; Auluck, S. The Influence of Oxygen Vacancies on the Linear and Nonlinear Optical Properties of $Pb_7O(OH)_3(CO_3)_3(BO_3)$. *RSC Adv.* **2017**, *7* (24), 14752−14760.
(20) Choi, E.; Lee, D.; Shin, H.-J.; Kim, N.; Valladares, L. D. L. S.; Seo, J. Role of Oxygen Vacancy Sites on the Temperature-Dependent Photoluminescence of SnO_2 Nanowires. *J. Phys. Chem. C* **2021**, *125* (27), 14974−14978.
(21) Menon, P. S.; Anjana, M. P.; Jose, A. K.; Kunjumon, J.; Aleena, P. A.; Chandran, S.; George, M.; Vinitha, G.; Sajan, D. The Role of Defects on Linear and Nonlinear Optical Properties of Pristine and Nickel Doped Zinc Oxide Nanoparticles. *Surf. Interfaces* **2022**, *34*, No. 102393.
(22) Pati, S.; Majumder, S. B.; Banerji, P. Role of Oxygen Vacancy in Optical and Gas Sensing Characteristics of ZnO Thin Films. *J. Alloys Compd.* **2012**, *541*, 376−379.
(23) Hohenberg, P.; Kohn, W. Inhomogeneous Electron Gas. *Phys. Rev.* **1964**, *136* (3B), B864−B871.
(24) Kohn, W.; Sham, L. J. Self-Consistent Equations Including Exchange and Correlation Effects. *Phys. Rev.* **1965**, *140* (4A), A1133−A1138.
(25) Kresse, G.; Furthmüller, J. Efficient Iterative Schemes for ab initio Total-energy Calculations Using a Plane-wave Basis Set. *Phys. Rev. B* **1996**, *54* (16), 11169−11186.
(26) Kresse, G.; Furthmüller, J. Efficiency of ab-initio Total Energy Calculations for Metals and Semiconductors Using a Plane-wave Basis Set. *Comput. Mater. Sci.* **1996**, *6* (1), 15−50.
(27) Kresse, G.; Hafner, J. Ab initio Molecular Dynamics for Liquid Metals. *Phys. Rev. B* **1993**, *47* (1), 558−561.
(28) Wang, V.; Xu, N.; Liu, J.-C.; Tang, G.; Geng, W.-T. VASPKIT: A User-friendly Interface Facilitating High-throughput Computing and Analysis Using VASP Code. *Comput. Phys. Commun.* **2021**, *267*, No. 108033.
(29) Perdew, J. P.; Burke, K.; Ernzerhof, M. Generalized Gradient Approximation Made Simple. *Phys. Rev. Lett.* **1996**, *77* (18), 3865−3868.
(30) Blöchl, P. E. Projector Augmented-wave Method. *Phys. Rev. B* **1994**, *50* (24), 17953−17979.
(31) Kresse, G.; Joubert, D. From Ultrasoft Pseudopotentials to the Projector Augmented-wave Method. *Phys. Rev. B* **1999**, *59* (3), 1758−1775.
(32) Grimme, S.; Ehrlich, S.; Goerigk, L. Effect of the Damping Function in Dispersion Corrected Density Functional Theory. *J. Comput. Chem.* **2011**, *32* (7), 1456−1465.
(33) Grimme, S.; Antony, J.; Ehrlich, S.; Krieg, H. A Consistent and Accurate ab initio Parametrization of Density Functional Dispersion Correction (DFT-D) for the 94 Elements H-Pu. *J. Chem. Phys.* **2010**, *132* (15), 154104.
(34) Becke, A. D. A New Mixing of Hartree−Fock and Local Density-functional Theories. *J. Chem. Phys.* **1993**, *98* (2), 1372−1377.
(35) Gajdoš, M.; Hummer, K.; Kresse, G.; Furthmüller, J.; Bechstedt, F. Linear Optical Properties in the Projector-augmented Wave Methodology. *Phys. Rev. B* **2006**, *73* (4), No. 045112.
(36) Baroni, S.; Resta, R. Ab initio Calculation of the Macroscopic Dielectric Constant in Silicon. *Phys. Rev. B* **1986**, *33* (10), 7017−7021.
(37) Jain, A.; Ong, S. P.; Hautier, G.; Chen, W.; Richards, W. D.; Dacek, S.; Cholia, S.; Gunter, D.; Skinner, D.; Ceder, G.; et al. Commentary: The Materials Project: A Materials Genome Approach to Accelerating Materials Innovation. *APL Mater.* **2013**, *1* (1), No. 011002.
(38) Saha, S.; Sinha, T. P.; Mookerjee, A. Electronic Structure, Chemical Bonding, and Optical Properties of Paraelectric $BaTiO_3$. *Phys. Rev. B* **2000**, *62* (13), 8828−8834.
(39) Murphy, A. B. Band-gap Determination from Diffuse Reflectance Measurements of Semiconductor Films, and Application to Photoelectrochemical Water-splitting. *Sol. Energy Mater. Sol. Cells* **2007**, *91* (14), 1326−1337.
(40) Viezbicke, B. D.; Patel, S.; Davis, B. E.; Birnie, D. P. Evaluation of the Tauc Method for Optical Absorption Edge Determination: ZnO Thin Films as a Model System. *Phys. Status Solidi B* **2015**, *252* (8), 1700−1710.
(41) Makuła, P.; Pacia, M.; Macyk, W. How To Correctly Determine the Band Gap Energy of Modified Semiconductor Photocatalysts Based on UV−Vis Spectra. *J. Phys. Chem. Lett.* **2018**, *9* (23), 6814−6817.
(42) Thomas, P. A. The Crystal Structure and Absolute Optical Chirality of Paratellurite, α-TeO_2. *J. Phys. C: Solid State Phys.* **1988**, *21* (25), 4611.

https://doi.org/10.1021/acs.jpcc.3c05472
J. Phys. Chem. C 2024, 128, 1728−1736

(43) Beyer, H. Verfeinerung der Kristallstruktur von Tellurit, dem rhombischen TeO_2. *Z. Kristallogr.* **1967**, *124* (3), 228−237.
(44) Champarnaud-Mesjard, J. C.; Blanchandin, S.; Thomas, P.; Mirgorodsky, A.; Merle-Méjean, T.; Frit, B. Crystal Structure, Raman Spectrum and Lattice Dynamics of a New Metastable Form of Tellurium Dioxide: γ-TeO_2. *J. Phys. Chem. Solids* **2000**, *61* (9), 1499−1507.
(45) Deringer, V. L.; Stoffel, R. P.; Dronskowski, R. Thermochemical Ranking and Dynamic Stability of TeO_2 Polymorphs from Ab Initio Theory. *Cryst. Growth Des.* **2014**, *14* (2), 871−878.
(46) Li, Y.; Fan, W.; Sun, H.; Cheng, X.; Li, P.; Zhao, X. Structural, Electronic, and Optical Properties of α, β, and γ-TeO_2. *J. Appl. Phys.* **2010**, *107* (9), No. 093506.
(47) Ceriotti, M.; Pietrucci, F.; Bernasconi, M. Ab initio study of the vibrational properties of crystalline TeO_2: The α, β, and γ phases. *Phys. Rev. B* **2006**, *73* (10), No. 104304.
(48) Moufok, S.; Kadi, L.; Amrani, B.; Khodja, K. D. Electronic Structure and Optical Properties of TeO_2 Polymorphs. *Results Phys.* **2019**, *13*, No. 102315.
(49) Beaudry, J.-N.; Grenier, S.; Amrate, S.; Mazzera, M.; Zappettini, A. Synthesis of High Purity, Stoichiometric Controlled, TeO_2 Powders. *Mater. Chem. Phys.* **2012**, *133* (2), 804−807.
(50) Takizawa, K.; Okada, M.; Ieiri, S. Refractive Indices of Paratellurite and Lithium Iodate in the Visible and Ultraviolet Regions. *Opt. Commun.* **1977**, *23* (2), 279−281.
(51) Baur, W. The Geometry of Polyhedral Distortions. Predictive Relationships for the Phosphate Group. *Acta Crystallogr. B* **1974**, *30* (5), 1195−1215.
(52) Walsh, A.; Payne, D. J.; Egdell, R. G.; Watson, G. W. Stereochemistry of Post-transition Metal Oxides: Revision of the Classical Lone Pair Model. *Chem. Soc. Rev.* **2011**, *40* (9), 4455−4463.
(53) Ohmachi, Y.; Uchida, N. Temperature Dependence of Elastic, Dielectric, and Piezoelectric Constants in TeO_2 Single Crystals. *J. Appl. Phys.* **1970**, *41* (6), 2307−2311.
(54) Keerthana; Rao, V. V.; Venimadhav, A. Tuning the Permittivity of Tellurium Dioxide by Ti Substitution. *Ceram. Int.* **2020**, *46* (7), 8827−8831.
(55) Boyd, R. W., Chapter 2 - Wave-Equation Description of Nonlinear Optical Interactions. In *Nonlinear Optics* (Fourth Edition), Boyd, R. W., Ed. Academic Press: 2020; pp 65−135 DOI: 10.1016/b978-0-12-369470-6.00002-2.
(56) Robertson, J. High Dielectric Constant Oxides. *EPJ. Appl. Phys.* **2004**, *28* (3), 265−291.

https://doi.org/10.1021/acs.jpcc.3c05472
J. Phys. Chem. C 2024, 128, 1728−1736